The 11th January 2018, Mw 6.0 Bago-Yoma, Myanmar earthquake: A shallow thrust event within the deforming Bago-Yoma Range

Wardah Fadil[1,2], Eric O. Lindsey[1], Yu Wang[3], Phyo Maung Maung[1], Heng Luo[4], Tint Lwin Swe[5], Pa Pa Tun[6], Shengji Wei[1,2]

[1]Earth Observatory of Singapore, Nanyang Technological University, Singapore

[2]Asian School of the Environment, Nanyang Technological University, Singapore

[3]National Taiwan University, Taiwan

[4]State Key Laboratory of Information Engineering in Surveying, Mapping, and Remote Sensing, Wuhan University, China

[5]Myanmar Earthquake Committee, Myanmar

[6]Department of Meteorology and Hydrology, Myanmar

Corresponding author: Shengji Wei (shjwei@ntu.edu.sg)

Wardah Fadil (wardahsh001@e.ntu.edu.sg)

Key Points: (<140 characters)

- We propose that the Mw6.0 Bago-Yoma earthquake ruptured a previously unmapped SW-dipping thrust fault at shallow depths within the Bago-Yoma Range anticlinorium.
- The upper crust of the Burma plate between the megathrust and Sagaing Fault is undergoing distributed deformation to partly accommodate the oblique convergence of the Indian plate.
- The proximity of mapped and potentially unidentified active faults within the Bago-Yoma Range to dams and reservoirs indicate an increased seismic hazard.

Abstract (250 words)

On 11th January 2018 (18:26 UTC), a Mw 6.0 earthquake occurred approximately 30 km west of the Sagaing Fault in the Bago-Yoma Range (BYR). Using a local broadband seismic network and regional seismic stations, we refine the source parameters of the earthquake sequence. We relocate ~100 earthquake epicenters and determine the focal mechanism and centroid depth of the mainshock and 20 aftershocks with Mw>4. The relocated epicenters are distributed in an elongated zone oriented in a NW-SE direction that is consistent with the strike of the mainshock fault plane solution and the slip distribution derived from ALOS-2 InSAR observations. Most of the aftershocks have a pure thrust focal mechanism similar to the mainshock, except for four strike-slip aftershocks. The refined source parameters of the thrust events clearly delineate a fault dipping ~40˚ to the southwest at a depth range of 3-7 km, indicating that the earthquake sequence ruptured a previously unmapped, active fault. We interpret the earthquake sequence to be associated with pre-existing faults within the BYR anticlinorium. This earthquake sequence and historical seismicity indicate that the upper crust of the BYR is highly stressed, resulting in ongoing distributed deformation between the oblique Rakhine megathrust and the dextral Sagaing Fault. The seismic hazard posed by these active faults has been increasing with the development of infrastructure such as dams within the BYR. Our study highlights the need for high-resolution earthquake source parameter and strong ground motion attenuation studies for seismic hazard preparation and further understanding of the neotectonics of Myanmar.

Plain Language Summary

Myanmar is known to host many earthquakes, where most of the large earthquakes in the past have occurred along the strike-slip Sagaing Fault and along the interface of or within the Indian plate that subducts beneath the Burma plate off the west coast of Myanmar. Less attention is given to smaller magnitude and shallower earthquakes that occur in the region between the subduction zone and the Sagaing Fault, due to lack of instrumentation to detect smaller earthquakes and their less destructive potential. The 2018 Mw6.0 earthquake occurred in this region within the Bago-Yoma Range (BYR) and was not associated with any mapped active faults. We use seismological and geodetic data in addition to historical earthquake records and existing geologic maps and surveys to study the earthquake. We propose that the earthquake occurred on an existing shallow thrust fault within the BYR, which ruptured due to the region accommodating part of the compression associated with the subduction, along multiple small-scale crustal faults. We also highlight the increased seismic hazard in the region due to the close proximity of these active faults to numerous dams.

1. Introduction

Myanmar is situated within a region of active tectonic blocks with boundaries defined by a variety of tectonic settings (Fig. 1a). The Burma sliver plate is characterized by the highly oblique convergence of the Indian plate (~18 mm/yr) at its western boundary while the ~N-S striking right-lateral Sagaing Fault (~20 mm/yr) defines its eastern boundary bordering the Shan Plateau on the Sunda plate (Socquet et al., 2006; Mallick et al., 2019). The Eastern Himalayan Syntaxis represents the northern termination of the Burma plate while the Andaman Sea spreading center separates the Burma sliver plate from the Sunda plate to the south. As a result, the seismicity in Myanmar is highly active, with most of the historical seismicity distributed along the plate-boundary-type Sagaing Fault, the Rakhine subduction zone, and within the subducting Indian slab (Fig. 1b). Therefore, a majority of the seismological and geological studies in the region have been focused on active structures associated with the subduction zone and the Sagaing Fault (Le Dain et al., 1984; Ni et al., 1989; Chen & Molnar, 1990; Steckler et al., 2008; Wang et al., 2013; Shyu et al., 2018).

While a significant amount of motion between the Indian and the Sunda Plate is accommodated by the aforementioned plate boundary faults, recent studies show that shallow earthquakes occur within the Central Myanmar Basin (CMB), indicating distributed deformation within the Burma Plate (Chit Tet Mon et al., 2020). This distributed deformation may be accommodated by numerous crustal faults, which are predominantly thrust faults close to the eastern edge of the Western Range (WR; also known as Indo-Burma Range), as evidenced by geological observations (e.g. Wang et al.., 2014). Although accurate slip rates of these crustal faults are still not available due to sparse GPS observations in southwest Myanmar, several damaging shallow earthquakes have occurred such as the 2003 Mw 6.6 Taungdwingyi strike-slip earthquake located ~48km to the west of the Sagaing Fault (Maung Thein et al., 2009), the 2007 Mw 5.6 NW-SE striking thrust earthquake (GCMT) on the western flank of the BYR, and two damaging earthquakes in 1858 and 1927 (e.g., Oldham, 1883; Chibber, 1934; Le Dain et al., 1984;, Hurukawa & Maung Maung, 2011; Wang et al., 2014) (Fig. 1b). With recent rapid economic growth and development of infrastructure (e.g. dams), the seismic hazard analysis in SW Myanmar has become more pressing. The Mw 6.0 earthquake that occurred on 11th January 2018 (18:26 UTC) in the southern Bago-Yoma Range (BYR) raises the alarm to a higher level.

The BYR is a NNW-SSE trending uplifted region within the southeastern part of the CMB with the major structural trend oriented sub-parallel to the Sagaing Fault (e.g., Bender, 1983). The highest elevation at its peak is ~550 m above sea level and is dwarfed in comparison to the WR to the west and the Shan Plateau to the east. The northwestern and southern segments of the BYR merge into the Salin and Prome subbasins, respectively (Pivnik et al., 1998). The BYR has been interpreted as an anticlinorium within the larger synclinorium of the Central Myanmar Basin, with outcrops exposing Miocene sandstones and shales (Naing Maw Than et al., 2017). Geomorphic and geological studies show predominantly NNW-SSE and NW-SE linear structures (Bender, 1983; Ridd & Racey, 2015; Sloan et al., 2017). Previous GPS studies in Myanmar lack data within this area, thus, making seismic data one of the few resources currently available to understand the ongoing deformation within the BYR.

Early reports (e.g. NEIC, GCMT, GFZ) of the 2018 mainshock indicate a source depth ranging from 9-12 km and a thrust focal mechanism on a 40˚- 50˚ dipping fault plane striking NNW-SSE, with 30 M>4 aftershocks as reported by NEIC. Yet, such a thrust fault at the mountainous epicenter region of the earthquake has not been mapped as an active fault, due to limited geological and geophysical observations. This earthquake sequence was well recorded by a broadband seismic network that was recently installed by the collaboration between EOS-DMH-MEC (Earth Observatory of Singapore – Department of Meteorology and Hydrology, Myanmar – Myanmar Earthquake Committee) and the Myanmar national broadband seismic network (Hrin Nei Thiam et al., 2017) (Fig. 1a). It provides a unique dataset for us to better constrain the source parameters of the earthquakes and therefore, better understand their tectonic implication, as well as the seismic hazards from such crustal faults.

In this study, we first use the P-wave arrival time recorded by the regional broadband network to relocate the epicenter of the earthquake sequence. We then apply a waveform inversion method to precisely determine the focal mechanism and centroid depth of the mainshock and 20 M >4 aftershocks that occurred between January – June 2018. The seismicity and fault geometry are then verified by a slip model derived from InSAR ALOS-2 data. This is followed by a discussion on the seismotectonic implications of our findings and the seismic hazard that this newly identified fault and other potential unidentified active faults pose due to their assumed inactivity and proximity to the dams and reservoirs.

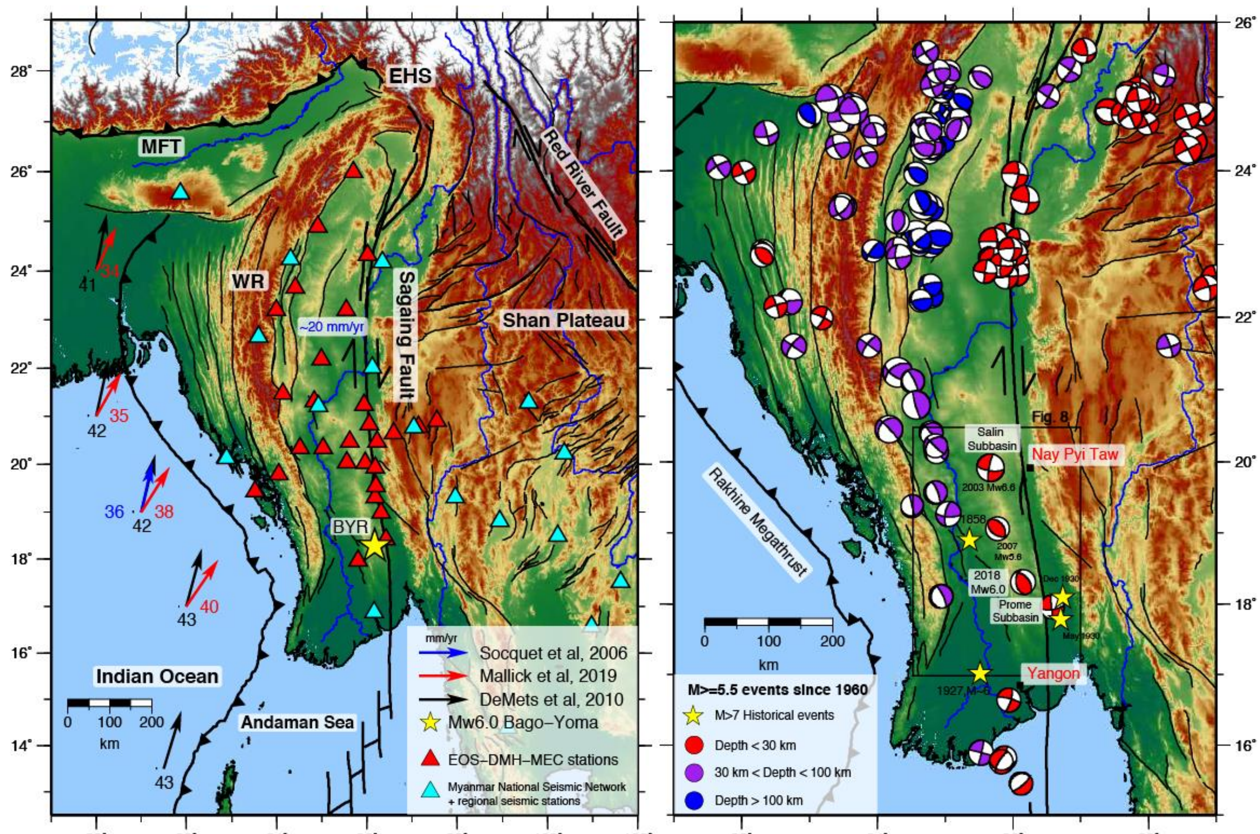

Figure 1. Regional tectonics and historical seismicity in Myanmar. (Left) Location of seismic stations in Myanmar used in this study. Arrows indicate motion of the Indian plate relative to the Shan Block/Plateau (red) and motion of the Indian plate relative to the Sunda plate (blue, black). Regional faults modified from Wang et al. (2014) and Taylor & Yin (2009) (black lines). (Right) Focal mechanisms of historical earthquakes (M>5.5) from global earthquake catalogs (Dziewonski et al., 1981; Ekstrom et al., 2012). Location of M>7 historical earthquakes (yellow stars) were obtained from Le Dain et al. (1984), Hurukawa & Maung Maung (2011) and Wang et al. (2014). MFT – Main Frontal Thrust, EHS – Eastern Himalayan Syntaxis, WR – Western Range, BYR – Bago-Yoma Range.

2. Data and Methods

2.1 Earthquake epicenter relocation and focal mechanism inversion

The Mw 6.0 mainshock occurred in the southern part of the BYR, ~30 km west of the Sagaing Fault and ~35 km southwest of Phyu city. Approximately 100 M_L >1.5 aftershocks were reported by the EOS-DMH-MEC seismic network. The earthquake sequence was well-recorded by the seismic network and at least 4 stations (M011, M012, M003, M004) recorded the mainshock and aftershocks within a distance of <100 km, allowing the P-wave arrival of aftershocks with M>1.5 to be well-identified at these stations. We tested various 1D velocity models extracted from CRUST1.0 (Laske et al., 2013) in both travel-time and waveform analysis and found that the model at (18.5˚N, 96.5˚E) (Fig. S1) performs the best. With this model, we relocated the epicenter of the mainshock and aftershocks using a grid-search technique. Assuming a source depth of 7 km, we searched for the best epicenter and origin time (t_0) for each event by minimizing the residual travel time between the data (*T_obs*) and the calculated P-wave travel time (*T_calc*) at each station *i* for *N=4* closest stations:

$$Error = \frac{1}{N}\sum_{i=1}^{N}(T\_obs_i - T\_calc_i - t_0)^2$$

To further refine the location of similar events within a cluster, we modified the method to locate events relative to a reference event. This is achieved by extracting station correction values to the P-wave travel time for the best earthquake location in the initial grid search and applying those values to the subsequent grid search relocation.

To determine the focal mechanism of the earthquakes, we adopted the generalized Cut-And-Paste (gCAP) waveform inversion method (Zhu & Helmberger, 1996; Zhu and Ben-Zion, 2013), which cuts the three-component (R,T,Z) waveforms into Pnl and Surface wave segments and fits them with synthetics from a given velocity model while allowing different time shifts for each segment. The inversion searches through the best combination of strike, dip and rake values to produce synthetics that minimize the error function and the inversion is repeated at a range of depth values to determine the best centroid depth. The synthetics were derived from a Green's function library calculated at a range of depths and epicentral distances from the earthquake source using the frequency-wavenumber integration method (Zhu & Rivera, 2002) and the same 1D CRUST1.0 velocity model used in the travel-time analysis. Routine waveform data processing was conducted prior to the analysis which include removal of instrument response and rotation of horizontal components to radial and tangential components.

For the Mw 6.0 mainshock, waveforms from nearly all EOS-DMH-MEC and Myanmar National Seismic Network broadband stations in Myanmar were used. To improve the azimuthal coverage, broadband stations in Thailand were also included

(CHTO, CMMT, CRAI). For the M>4 aftershocks, we included as many regional stations as possible with good signal-to-noise ratio in the inversion. The inversion was conducted at a frequency range of 0.02 – 0.08 Hz for the Pnl segments and 0.02 – 0.06 Hz for the surface wave segments. We removed waveform segments that were clipped and excluded complicated waveforms at stations close to the coast and located on thick sediments. The inversion was repeated at 1 km intervals for a shallow depth range of 1-20 km.

Depth is a critical source parameter to define the fault geometry with seismicity. To verify the centroid depths obtained from the gCAP inversions, we further inspected the amplitude ratios between the Pnl waves and surface waves. The surface-/Pnl-wave amplitude ratio for earthquakes recorded at a nearby station should decrease as the depth of the earthquake increases, assuming the radiation pattern of the earthquakes are similar. We selected a subset of similar thrust-faulting aftershocks that are located within 2 km of the AA' profile, which is perpendicular to the strike of the fault. We plotted the surface-/Pnl-wave amplitude ratio of these events as a function of distance from station M011 (Fig. 5a). The depth phases of these events at the M011 station were also examined to verify the depths (Fig. 5b).

2.2 InSAR observation and inversion

To determine the surface deformation caused by the earthquake, we processed L-band interferometric synthetic aperture radar (InSAR) data collected by the ALOS-2 satellite operated by the Japanese Aerospace Agency (JAXA). The L-band data collected by this satellite works well in densely vegetated or forested areas such as the BYR; we also processed C-band data collected by the European Space Agency's Sentinel-1 satellite but found that it did not maintain sufficient interferometric coherence to map the deformation. We used the ALOS-2 wide-swath interferometric pair collected on 2017/12/26 and 2018/3/06 along descending Path 41, Frame 3250. We processed the data using GMTSAR software (Sandwell et al.., 2011), with topographic corrections from the Shuttle Radar Topography Mission Global 1 arc second dataset (SRTMGL1; NASA JPL 2013), and unwrapped the phase using Snaphu (Chen & Zebker, 2000). We removed long wavelength artifacts from the interferogram using a highpass gaussian filter with a wavelength of 100 km and removed topographically-correlated atmospheric noise using a simple linear regression. To reduce the high-resolution image to a more feasible number of observation points for modeling, we downsampled the data using a variance-based quadtree algorithm (Simons et al.., 2002) with a variance threshold of 12 mm. The original and detrended interferograms and the final set of resampled points are shown in Fig. S2. We then applied an inversion algorithm proposed by (Jónsson et al.., 2002) to the downsampled data to determine the static slip distribution on the fault. The same 1D velocity model as used in the waveform inversion was used to compute the static Green's function library. We attempted the inversion on both possible fault planes.

3. Results

3.1 Epicenter relocation and focal mechanism inversion

The epicenter relocation results in an elongated cluster of earthquakes striking NW-SE with dimensions of ~20km long and ~8 km wide, located in between the strike-slip Sagaing Fault to the east and the reverse Paungde Fault and West Bago Yoma Fault to the west (Fig. 2). The epicenter relocations converge into a tighter cluster compared to their initial locations. The relative horizontal location uncertainty is as small as ~1km, given the close proximity of the seismic stations (<100km) (Fig. S3). Observations of ground displacement from InSAR data (ALOS-2, descending) show that the epicenter relocations overlap with the area of maximum ground displacement, which also has an elongated NNW-SSE striking orientation, thus validating the accuracy of our epicenter relocations (Fig. 2c). The lack of a post-earthquake field survey means we cannot confirm whether the fault ruptured to the surface or not, however, the gradual shifts in the deformation pattern of the InSAR data (Fig S2) indicate that the rupture did not reach to the surface. This is later verified by the static slip inversions.

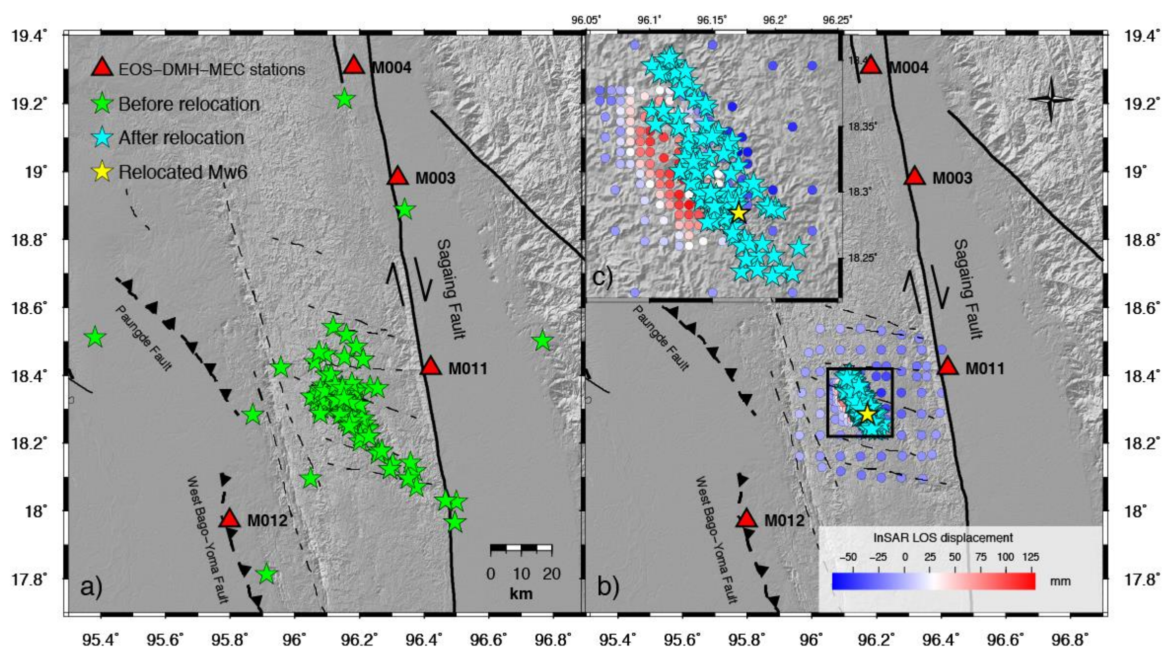

Figure 2. Earthquake relocation results using grid-search technique. (a) Initial epicenters of mainshock and ~100 aftershocks. Red triangles represent location of the four closes seismic stations used in the relocation process. (b) Relocated epicenters clustered in a NW-SE elongated trend within the BYR, consistent with the observed pattern of maximum ground displacement indicated by InSAR ALOS-2 ground displacement (colored circles). (c) Zoomed in plot of the black square rectangle, showing the distribution of epicenters and InSAR ground displacement. Solid and dashed black lines are active and inferred faults from Bender, 1983 and Wang et al., 2014.

The waveform inversion for the Mw 6.0 mainshock results in a thrust-faulting focal mechanism (strike=130˚/334˚, dip=40˚/53˚, rake=71˚/105˚), in which the strike values are consistent with NW-SE strike of the fault inferred from epicenter relocation and InSAR observations (Fig 3a and 4) . The surface wave segments for the four closest stations (M011, M012, M003, M004) are excluded from the inversion due to the waveforms being clipped. The grid search results for the depth indicate that the mainshock occurred at a shallow depth of 4.8 km (Fig. 3b). At the selected frequency range (see Fig. 3), the inversion results in good waveform fits between data and synthetics for stations <500 km from the epicenter. However, waveform segments from several stations are too complicated to be well-fit by the 1D velocity model and are tuned off in the inversion. These stations are either located near the coastline or within the central Myanmar basin on top of thick layers (up to 18 km) of sediment (Pivnik et al., 1998). The depth search result is shown as a plot of normalized error values as a function of depth and is well-resolved at this frequency range, which shows a sharp convergence at the best depth (Fig. 3b).

The inversion of 16 aftershocks with M >4 located within 6 km of the mainshock also show similar thrust-faulting mechanisms as the mainshock with depths ranging from 3-7 km. The shallowest thrust-faulting aftershock has a similar focal mechanism as the mainshock (strike=140˚/320˚, dip=48˚/42˚, rake=90˚/90˚) and is located about 1 km northeast of the mainshock at a depth of 3.9 km (Fig 3b, c). The deepest thrust-faulting aftershock (strike=122˚/347˚, dip=48˚/52˚, rake=56˚/55˚) is located at about 2 km southwest of the mainshock at a depth of 6 km (Fig. 3b, d). The waveform fits for these events are also good for stations <500 km away and the depths are well-resolved (also see Fig. S4). We observe that the ratio between the Pnl and surface wave segments of station M011 are larger for the shallower aftershock than the deeper aftershock (Fig. 3c,d). We also note that at these selected stations, the amplitude ratios between Sv and Sh waves are different between the two events. Excellent fits between the synthetics and observations provide strong constraints to both the focal mechanism and depth

Interestingly, the inversions show that four aftershocks are strike-slip events. Three of these strike-slip events occur as a cluster at slightly larger depths (7-8 km) than the thrust events, located at about 2 km to the east of the mainshock epicenter. Approximately one month after the mainshock another strike-slip aftershock occurred at ~6 km to the northwest of the mainshock epicenter. The largest (Mw4.5) strike-slip event has an almost pure strike-slip focal mechanism (strike=189˚/98˚, dip=82˚/85˚, rake=-175˚/-8˚) and is located at a depth of 6.8 km (Fig 3b, e). The amplitude ratio between the tangential component and Pnl component is clearly larger for these strike-slip events compared with the thrust events, despite their depth being a few km larger. Although the waveform fits to a few Pnl wave segments (e.g. M003) for the strike-slip events are slightly worse than that for the thrust events, the fits to the other components are quite decent to conclude that a cluster of strike-slip aftershocks occurred to the east of the mainshock at deeper depths than the thrust events. Complete waveform fit results for all stations and depth inversion plots are shown in Fig. S4a-d.

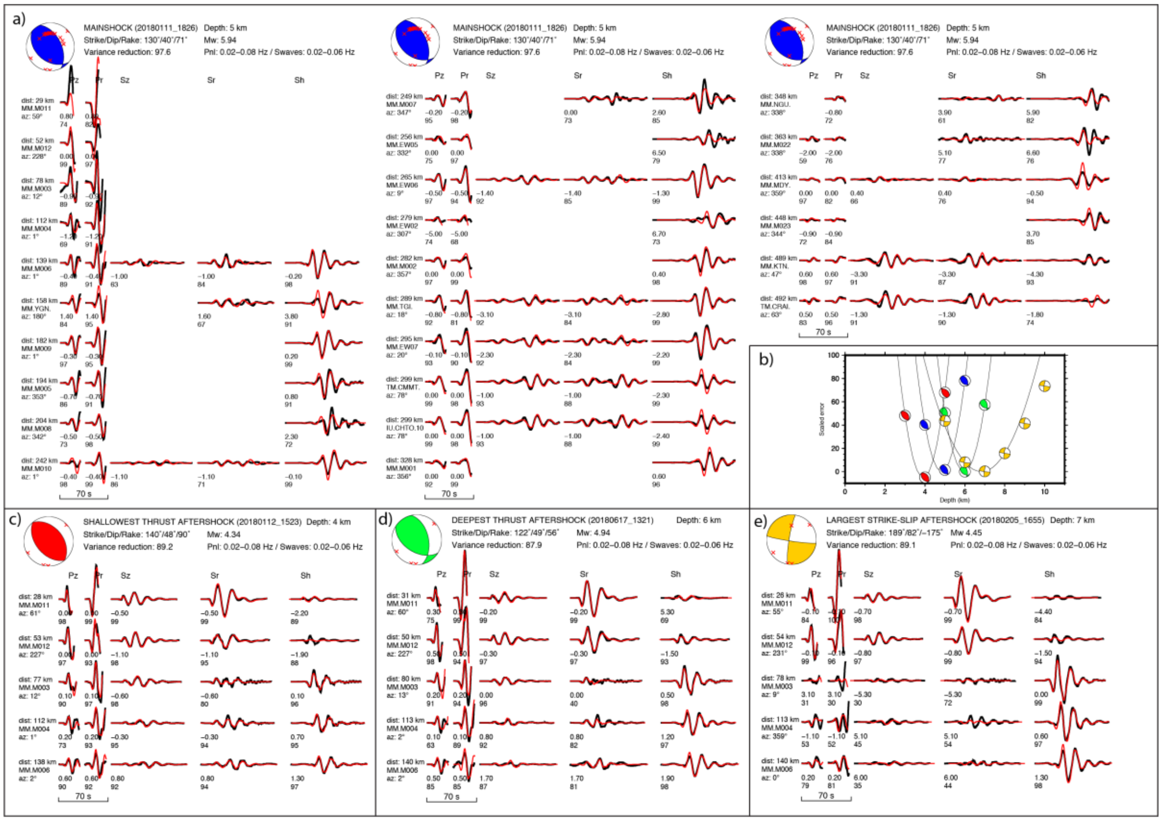

Figure 3. Cut-And-Paste inversion results. (Top panel) (a) Waveform fits between synthetics (red) from best the focal mechanism and the observed waveform (black) for the Mw6.0 mainshock. The best focal mechanism is shown in the top left. Station name is indicated at the leftmost column, along with its distance and azimuth from the epicenter. The waveform segments from left to right are as follows: Pnl – Z component, Pnl – Radial component, S-waves – Z component, S-waves – Radial component, S-waves – Tangential component. The first number below each waveform segment indicates the time shift (sec) followed by the waveform cross-correlation coefficient (%). (b) Plot of errors for various depth normalized to the minimum error, showing the best depth for the mainshock at ~4.8km. (Bottom panel) CAP inversion results for the shallowest (3.9 km) thrust aftershock (c), deepest (6.0km) thrust aftershock (d) and largest strike slip aftershock (e).

With the refined earthquake locations and source parameters, we can clearly see a lineation of the thrust events along a fault that dips ~40˚ in the depth profile (A-A') (Fig. 4), which is highly consistent with our point source focal mechanism solution for the Mw 6.0 mainshock. This seismicity profile suggests that the mainshock ruptured a SW-dipping fault. A list of the inverted source parameters for the mainshock and aftershocks is shown in Table 1.

Table 1: Focal mechanisms, centroid depth, moment magnitude of mainshock and 20 M>4 aftershocks from CAP inversion.

No.	Date	Time (UTC)	Lon	Lat	Nodal Plane 1 (Strike/Dip/Rake)	Nodal Plane 2 (Strike/Dip/Rake)	Depth (km)	Mw
1.	2018/01/11	18:26:24	96.171	18.284	130/40/71	334/53/105	4.8	5.94
2.	2018/01/11	20:08:41	96.148	18.327	268/50/43	147/59/131	2.0	4.09
3.	2018/01/12	15:23:55	96.169	18.293	140/48/90	320/42/90	3.9	4.34
4.	2018/01/12	04:16:03	96.128	18.326	130/61/90	310/29/90	4.0	4.19
5.	2018/01/13	23:29:47	96.138	18.319	139/50/64	356/46/118	4.2	4.20
6.	2018/01/13	13:51:15	96.130	18.324	310/29/82	139/61/94	4.3	3.93
7.	2018/01/14	17:49:56	96.131	18.343	101/71/-8	194/82/-161	4.6	4.35
8.	2018/01/17	07:43:27	96.133	18.319	323/37/77	159/54/100	5.5	4.01
9.	2018/01/22	07:37:59	96.141	18.299	322/67/67	189/32/133	4.0	4.31
10.	2018/02/05	16:55:35	96.192	18.288	189/82/-175	98/85/-8	6.8	4.45
11.	2018/02/07	16:38:01	96.203	18.286	101/79/-4	192/86/-169	8.2	4.10
12.	2018/02/09	18:04:25	96.197	18.287	109/82/1	19/89/172	8.0	4.03
13.	2018/03/04	10:48:10	96.176	18.265	336/48/112	125/46/67	4.8	4.54
14.	2018/03/17	19:59:04	96.152	18.290	328/40/82	158/50/97	5.8	4.63
15.	2018/04/20	22:29:24	96.164	18.277	128/42/64	341/53/112	5.1	4.87
16.	2018/04/20	04:16:02	96.159	18.280	121/51/59	345/48/122	5.2	4.53
17.	2018/04/21	22:41:11	96.160	18.280	119/50/51	351/54/127	5.0	4.40
18.	2018/04/22	18:31:44	96.170	18.290	330/47/100	136/44/80	4.1	4.53
19.	2018/04/24	12:23:34	96.151	18.282	120/50/59	343/49/122	5.3	4.82
20.	2018/06/17	13:21:31	96.151	18.278	122/49/56	348/51/123	6.0	4.94
21.	2018/06/17	13:42:35	96.146	18.277	310/70/61	188/35/143	6.7	4.04

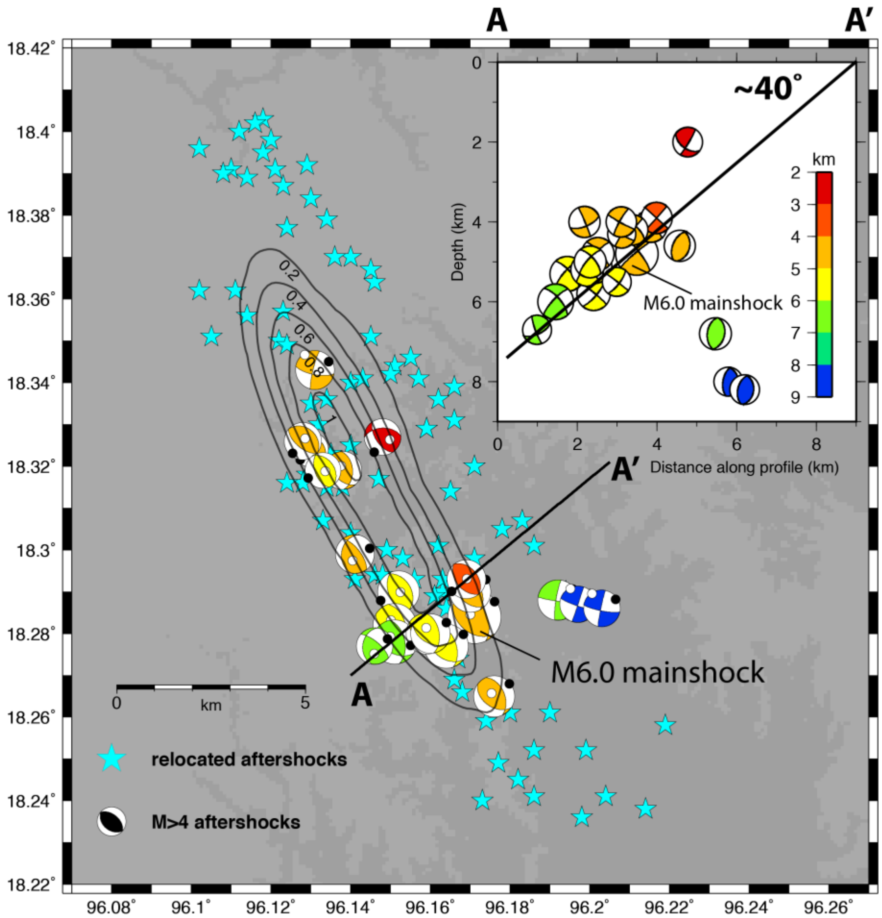

Figure 4. Relocated epicenters of mainshock and ~100 aftershocks and focal mechanisms of 20 M>4 aftershocks. Focal mechanisms are colored by depth. Black circles represent P-axis and white circles represent T-axis. Black contours represent coseismic slip derived from static slip inversion. (Inset) Cross-section plot along A-A', indicating a thrust fault dipping ~40° to the southwest rupturing at a depth range of (~3-6 km) and a strike-slip fault rupturing at a deeper depth of (~7-8 km).

3.2 Surface-/Pnl- wave amplitude ratio and depth phase analysis

To further validate our depth inversion results and the inferred fault geometry, we look at the surface-/Pnl-wave amplitude ratios and the possible depth phases of nine thrust-faulting aftershocks along the profile A-A'. The plot of surface-/Pnl-wave amplitude ratio as a function of distance from station M011 for these aftershocks show that despite their slightly smaller distances, the shallower events indeed have larger amplitude ratios (inset in Fig 5a). This supports our depth inversion results, since shallower events generate larger amplitude surface waves relative to the body waves.

We also produced record-sections of six thrust aftershocks at the closest station (M011, 28-30 km away from the events) (Fig 5, right panel). The waveforms for each event are aligned at the P-wave arrivals and sorted by distance from the station (closer events are shallower). Although it is difficult to model these broadband waveforms with a 1D velocity model, we can still identify the second largest peak after the P-arrival (~2 seconds after) as a possible depth phase (sP) and observe its moveout in the record section. The event with the shallowest depth (20180112_1523: 3.9 km), which is closest to the station, has the earliest depth phase arrival, while the deepest event (20180617_1321: 6 km), which is the furthest from station M011, has the latest depth phase arrival. This moveout is consistent with the depth variation we obtained from the focal mechanism inversion. The arrivals of the S-wave relative to P-wave also increase as a function of distance. Even though the observed moveouts occur over a duration of less than one second and requires careful picking of the P-wave arrival, it is consistent with the spatial distribution of the events that span a horizontal distance range of ~3 km and a vertical distance range of ~2km.

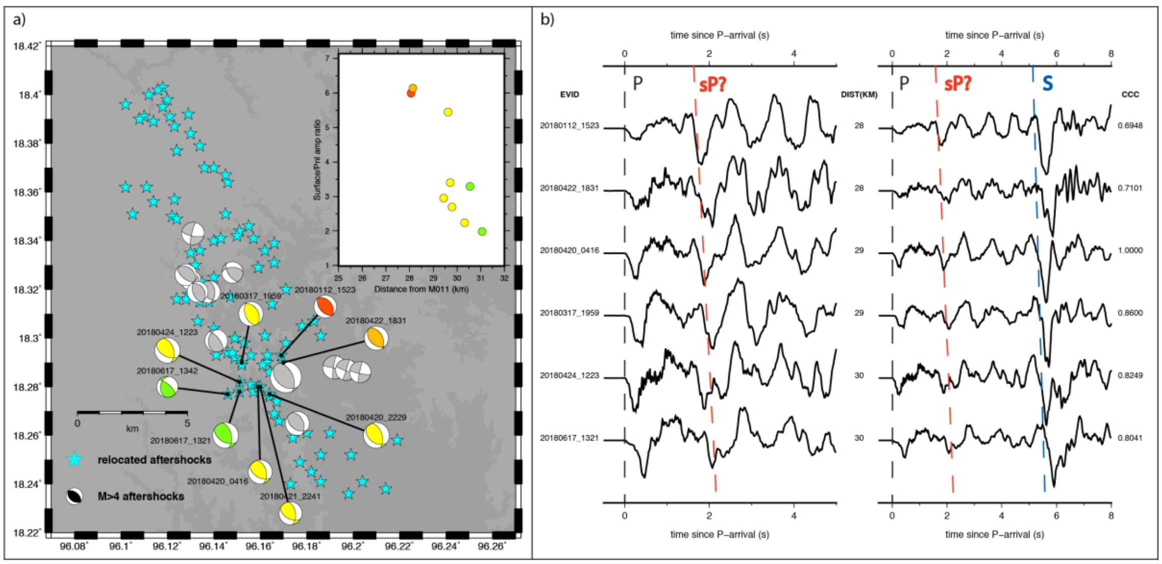

Figure 5. Depth analysis of M>4 thrust aftershocks. (a) Plot of focal mechanisms similar to Fig. 4 but with earthquakes included in the depth analysis indicated by focal mechanisms colored by depth. (Inset) Plot of Surface-/Pnl-wave amplitude ratio against the distance from the nearest station M011 for the selected focal mechanisms, showing a decreasing Surface-/Pnl amplitude ratio with increasing distance from M011, indicating a deeper source depth with increasing distance from the station. (b) Waveforms of the selected aftershocks aligned by the P-arrival time. The event name, distance from station M011 and cross-correlation coefficient of each waveform with event 20180420_0416 are indicated. The high cross-correlation coefficient values support the similarity of the epicenter and source mechanism of each thrust aftershock. The potential depth phase (sP) is indicated and shows a moveout with increasing distance from station M011, supporting a deeper source depth with increasing distance from the station.

3.3 Relative relocation of strike-slip earthquake cluster

Located at ~2km to the east of the mainshock epicenter, three of the four events with strike-slip focal mechanism form a sub-cluster of the seismicity. To determine which nodal plane is the ruptured fault, we further refined the location of the aftershocks within this sub-cluster relative to the location of the largest strike-slip aftershock (20180205_1655) (Fig. 6). The relative P-wave arrival times at station M011 and M012 between all five events in this cluster directly shows the sensitivity to the event location (Fig. 6a-c), where the event nearest to station M011 (20180207_1638) has the earliest P-arrival while the event furthest from M011 (20180205_1655) has the latest P-arrival and vice versa at station M012. The largest axis of the error ellipse in the grid search results indicates that the location uncertainty is well-constrained to within 1km (Fig 6d-i). These three events align nicely along the strike (98˚) of one of the fault plane solutions (Fig. 4e, Table 1), indicating that the near E-W oriented strike-slip fault had ruptured during the sequence, which is almost perpendicular to the active faults that were recently found in northern Myanmar (Chit Tet Mon et al.., 2020). The northernmost strike-slip event suggests that the rupture happened on another strike-slip fault that is probably parallel to the fault defined by the other three strike-slip event. Note that these strike-slip faults are almost perpendicular to the Sagaing Fault.

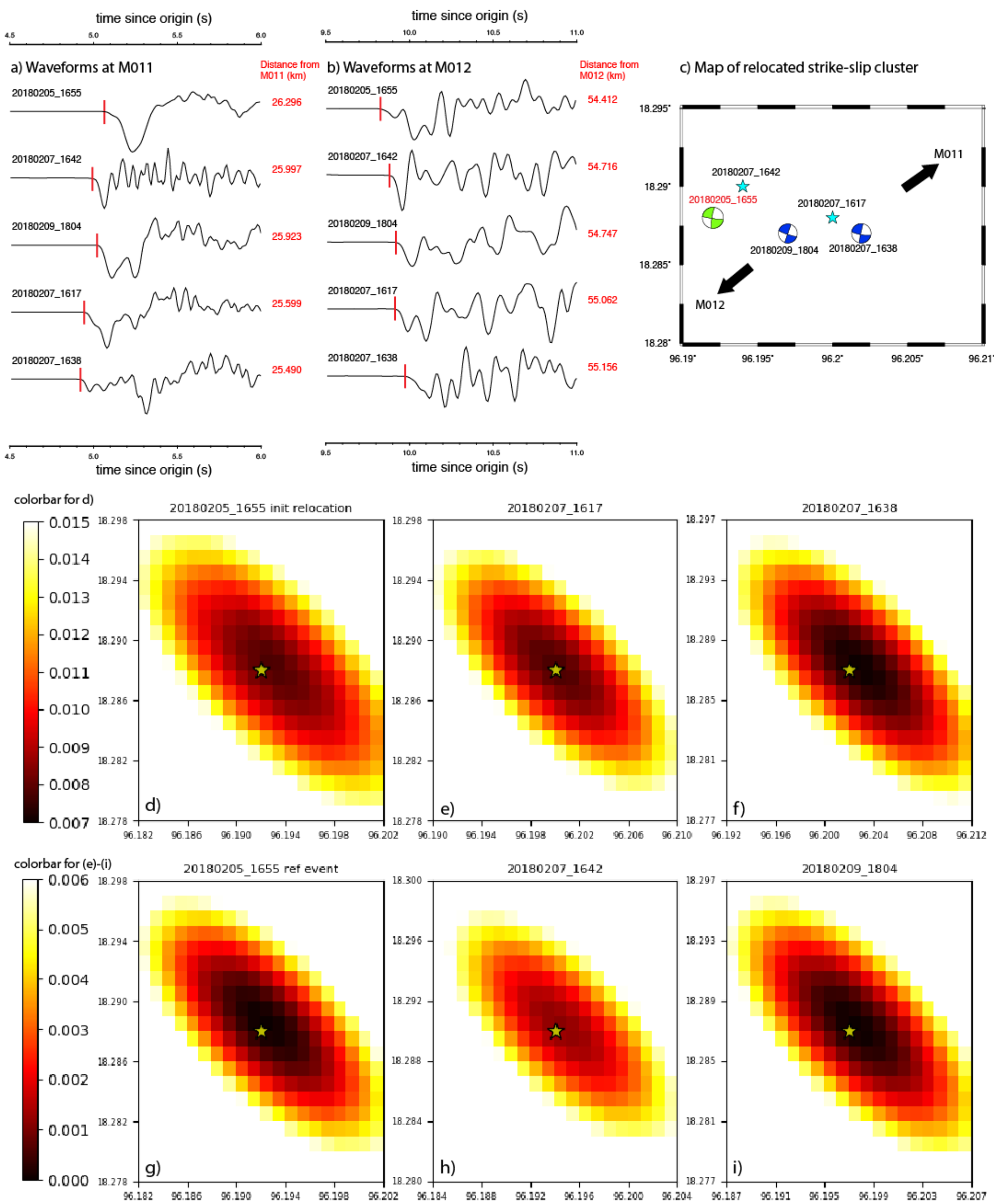

Figure 6. Strike-slip cluster indicate mainshock triggered an ~E-W trending left-lateral fault to the east of the mainshock epicenter. (a-b) Waveforms of the 5 events in the cluster at station M011 and M012, showing the increasing P-wave arrival time (red line) with increasing distance from each station. (c) Location of relocated aftershocks

relative to the reference event (20180205_1655). (d) L2-error plot for the initial grid search relocation of the reference event. (e-i) L2-error plot for events in the cluster after applying station correction values to the grid search.

3.4 Static slip inversion

The static slip models derived from both ascending and descending InSAR data for two possible fault planes are presented in Fig. 7 (southwest-dipping fault) and Fig S5 (northeast dipping fault). The inversion results show that both fault planes can fit the data almost equally well. Although the northeast dipping fault can fit the data slightly better, the difference in misfit is so small (1.68 cm vs 1.50 cm) that it could be ignored considering the other uncertainties (e.g. 3D structure). The southwest dipping fault plane inversion prefers a fault geometry that strikes 157° and dips 49°, highly consistent with the fault geometry from waveform inversion and seismicity alignment. The static moment (Mw5.95) also agrees well with the seismological moment (Mw6.0). The slip distribution shows an elongated rectangle shape that extends ~12km along strike and ~5km along dip, centroid at a depth of 5km, which is also very consistent with seismological results. Note that although the centroid depth is very shallow, the slip did not reach to the surface, with the top 3 km remaining un-ruptured. The along-strike length of slip distribution is fairly consistent with the seismicity distribution.

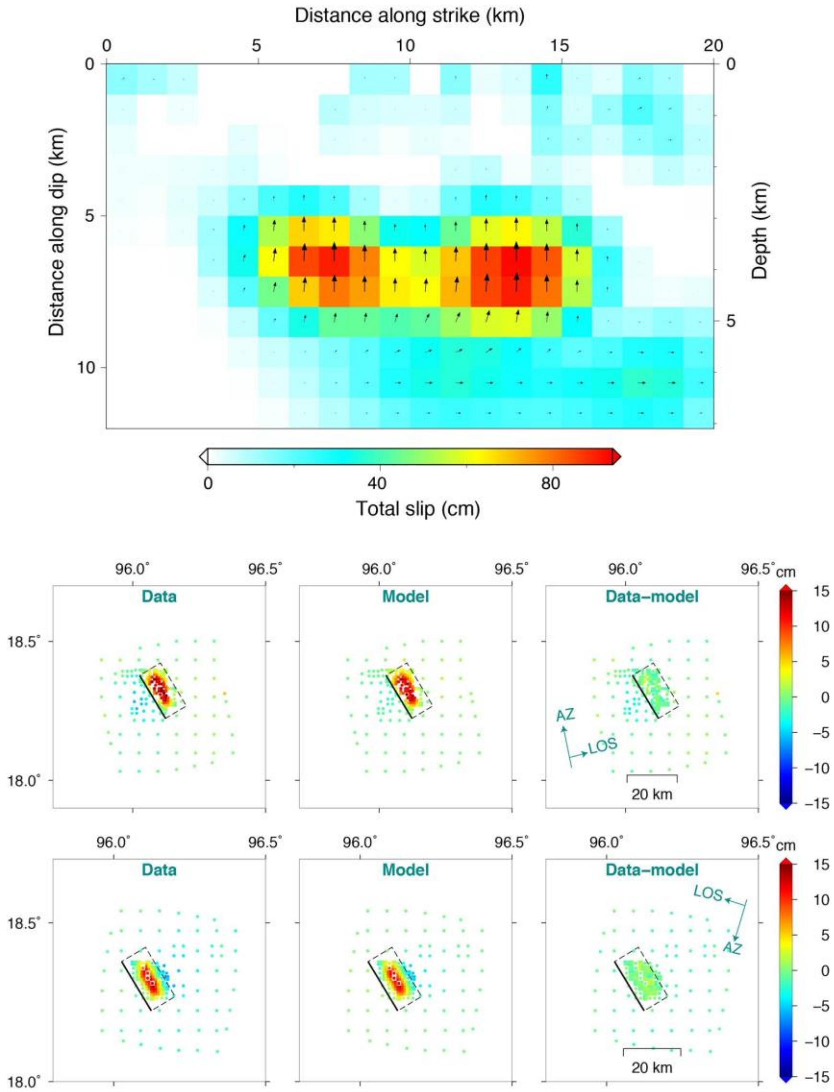

Figure 7. Static slip model and InSAR data fitting. The top panel shows the slip model in depth and along dip profile. The InSAR data fitting for the ascending (upper) and descending (lower) tracks are showed in the lower panel.

4. Discussion

4.1 Unmapped active faults in the upper crust and interpretations

Although previous studies have mapped faults and lineaments oriented NW-SE and NNW-SSE in the BYR from satellite imagery, the sense of motion and slip rate of these faults have yet to be confirmed (Bender, 1983; Taylor & Yin, 2009; Wang et al., 2014; Rangin, 2017; Sloan et al., 2017). It is noteworthy that the ruptured fault of the 2018 sequence is not associated with any mapped active thrust faults that have been previously identified. Historical earthquakes in the region reported by global earthquake catalogs show that there has not been a M>4.5 event within 30 km of the proposed ruptured fault. However, there have been several M>4.5 shallow thrust-faulting events located to the northwest of the recent Mw 6.0 earthquake, with similar focal mechanisms, such as the events in 2003, 2007 and 2013 (Fig. 8). In addition, we conducted focal mechanism inversions for several M>4 events in other regions along the western BYR outside of the 2018 Mw6.0 aftershock region (beachballs without year label in Fig. 8). Intriguingly, these shallow events also show thrust-faulting focal mechanisms similar to that of the 2018 event (Fig. 8). Note that the GCMT/USGS solutions in general have greater depth (15-20 km) than our solutions (~5km). This is due to the lower depth resolution in these global earthquake catalogs since they either use very long period for waveform inversion or did not have nearby stations to suppress the origin time-depth tradeoff. The P-axis direction from both strike-slip and thrust events all show an orientation of NE-SW, which is consistent with the plate convergence direction of the Indian plate relative to the Burma plate. In any case, these events are also not associated with any mapped active faults. The shallow crustal events in this region occurring on previously unidentified crustal structures may indicate that the very shallow part (a few km) of the upper crust of the Burma Plate is actively deforming, and possibly accommodating the distributed stresses due to the oblique subduction of the Indian plate beneath the Burma Plate off the west coast of Myanmar (Fig. 1).

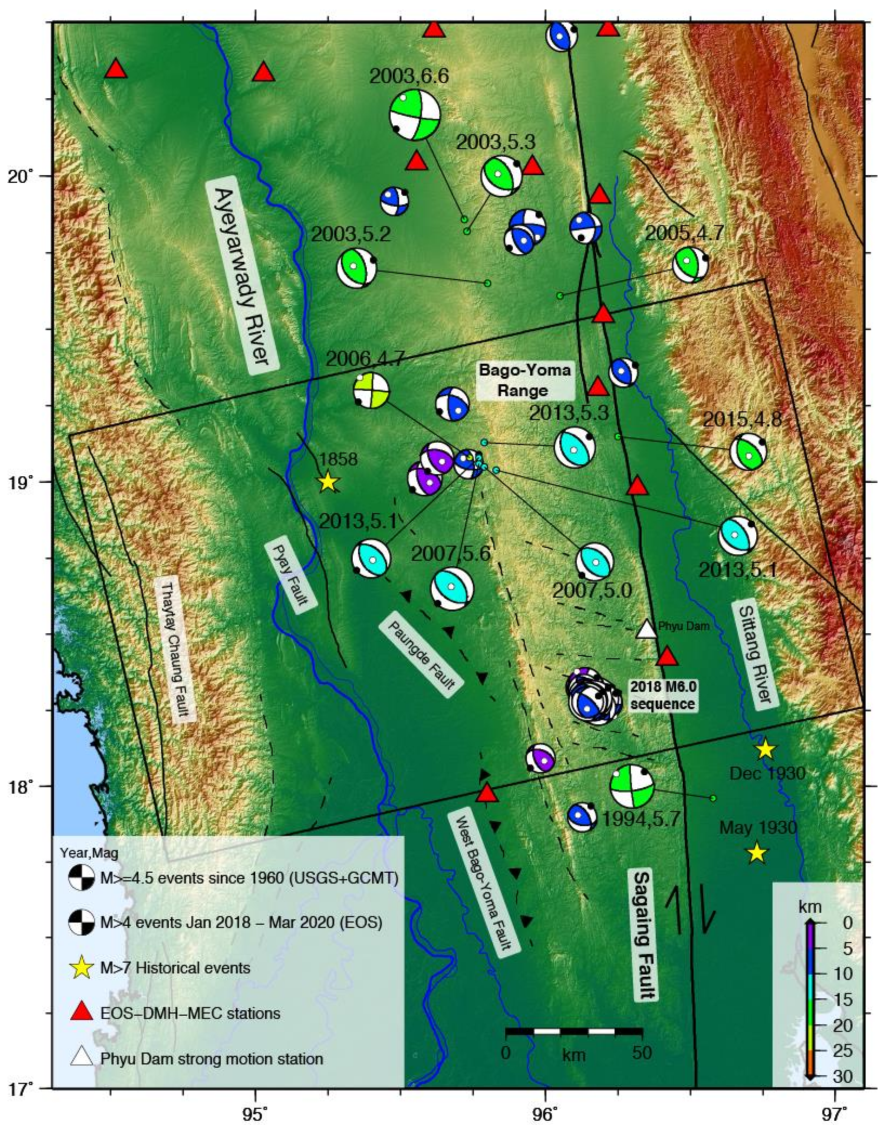

Figure 8. Crustal seismicity in the Bago-Yoma Range. M>4 earthquakes (<30 km deep) within and surrounding the Bago-Yoma Range from global earthquake catalogs (focal mechanisms with year and magnitude labeled) and our inversion of events recorded by the EOS-DMH-MEC stations (Jan 2018 – Mar 2020). We observe a trend of NW-SE striking thrust/oblique events along the BYR with occasional NS-EW striking strike-slip events.

Previous publications have offered various hypotheses to explain the tectonic history of the Central Myanmar Basin (CMB) and southern Myanmar, within which the 2018 sequence occurred. Pivnik et al. (1998) used petroleum exploration data to show that the Salin sub-basin is a synclinorium containing anticlines associated with the late-Miocene inversion structures, thrust sheets and low-relief uplifts. Bertrand and Rangin (2003) proposed that a regional plate kinematic reorganization occurred during the

Miocene which served as a transition between the transtensional tectonic regime related to the opening of the CMB and the transpressional tectonic regime related to the inversion of the CMB. Along the eastern CMB, Naing Maw Than et al. (2017) suggested that the area underwent two tectonic phases; a compressional phase during the late Miocene that formed the anticlines and synclines in the Pegu formations, followed by strike-slip movement along the Sagaing Fault that resulted in en echelon faulting. In general, most authors agree that the inner Burma plate has been subjected to approximately E-W compression since the late-Miocene, which formed the structures observed in and around the CMB. We observe that the P-axes of the thrust and strike-slip events (Fig. 8 and 9) are in agreement with such compressional background stress in the crust. Previous GPS observations also provide insights into the nature of deformation west of the Sagaing Fault. Socquet et al.. (2006) reveals that the Sagaing Fault only absorbs a portion of the deformation between the western coast and Shan Plateau at the latitude of 2018 earthquake (Fig.9 inset). The remaining deformation is primarily distributed between the Sagaing Fault and the western coast at a rate of ~13mm/year in the NNE direction, within which the BYR is located (Fig. 9, blue vector). We believe that the 2018 Mw 6.0 earthquake is a result of the NE-SW shortening being accommodated by a shallow thrust fault within the BYR, while the remaining deformation should be distributed on other secondary faults, such as the West Bago Yoma Fault, Paungde Fault and other unmapped faults, although the slip-rate of these faults are not yet known. To further understand the geodynamics and geologic history of this oblique subduction zone system, it is crucial to integrate geodetic and geologic observations along with detailed and robust earthquake source parameters as presented here to produce a more comprehensive and in-depth picture of the neotectonics.

Although there have been extensive oil and gas exploration efforts in the Central Myanmar Basin, there is a lack of published seismic reflection data in the BYR region due to the low hydrocarbon potential as indicated by surface geology (Ridd & Racey, 2015). Therefore, we are unable to compare our inferred thrust fault to structural maps or seismic-reflection data in the southern BYR area. However, we can place our interpreted fault geometry in a larger tectonic context of the Central Myanmar Basin by comparison with the structural maps and seismic lines available further to the north and south of the BYR (e.g., Pivnik et al., 1998; Ridd & Racey, 2015). Geologic cross-sections at latitudes of ~20˚-21˚N show that both east- and west-dipping thrusts occur in this region, produced by the inversion of the normal faults in the Salin synclinorium (see Fig. 2 in Pivnik et al., 1998). Some of these thrusts truncate the Plio-Pleistocene Irrawaddy formation, and their structural styles can be interpreted as positive flower structures. Their seismic profiles also reveal anticlines to the west of BYR. Geologic cross-sections at latitudes of ~16.5˚-17.5˚N also show both a large (~50km) and small (~10km) anticlines at ~50km to the south of recent earthquake (see Fig. 4.23, 4.24 in Ridd & Racey, 2015). Since double-vergence faults are common features found in many inverted sediment basins (e.g., Shinn, 2015; Pace & Calamita, 2014), and geological profiles north and south of our study area both shows east- and west-dipping faults with regional late-Miocene basin inversion history, we therefore suggest the fault that ruptured during the Mw 6.0 Bago-Yoma earthquake is also associated with a pre-existing southwest-dipping fault within the CMB area (Fig. 9). As the hypocenters of the Mw 6.0 earthquake sequence are limited at a shallow depth range of 2 to 7 km, and previous studies suggest that the main fault system at the western flank of BYR dips to the northeast (e.g. Wang et al., 2014), we further suggest that the ruptured southwest-dipping fault serves as the secondary fault in the push-up structure, and links to the main east-dipping fault at depth.

Unlike the thrust-type aftershocks, the source of the strike-slip aftershocks is less clear under the regional geological context. The four strike-slip aftershocks not only occurred in the footwall of the rupture fault, but also with fault orientation almost normal to the strike of the Sagaing Fault and other regional structures. As shown in geological maps of the BYR region (Naing Maw Than et al., 2017), and subsurface data of CMB area from Pivnik et al.. (1998), the primary structures with both areas are intercepted by a series of shorter faults with E-W orientations. These cross faults within the BYR and CMB area may act as the conjugate faults co-developed with the primary inversion structures since the beginning of the oblique plate convergence. Although these structures are relatively minor, the stress-change from the Mw 6.0 mainshock may trigger the slip of the nearby cross faults and produce these deeper strike-slip aftershocks.

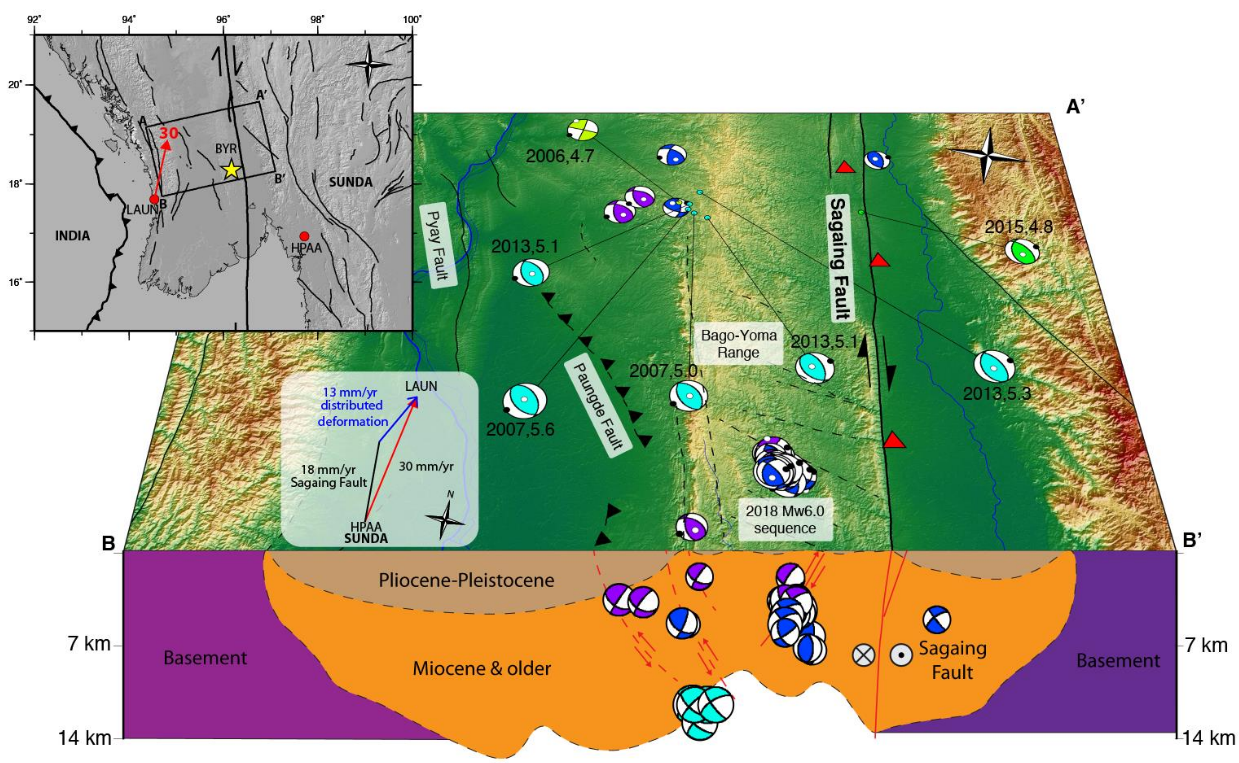

Figure 9. **Interpretation of deformation within the Bago-Yoma Range**. Schematic profile of the region at the location of the Mw6.0 earthquake sequence, modified from Ridd & Racey, 2015. (Inset) GPS velocity vector of LAUN with respect to HPAA/Sunda (red vector) and velocity diagram showing distributed deformation across southern Myanmar (blue vector), modified from Socquet et al., 2006.

4.2 Dams and seismic hazard

Due to its rugged topography, the BYR is sparsely populated and remains as a dense forested area. Therefore, it serves as a rainwater-catchment area with channels feeding into the southward flowing Ayeyarwady River to the west and the Sittang River to the east (Fig. 10). There are numerous dams within the BYR, located along the Sagaing Fault and along the eastern edge of the Western Range (Fig. 10). In the vicinity of the 2018 Mw6.0 earthquake, there are several major dams ~25-35 km to the north (e.g. Kun Dam, Phyu Chaung Dam) and south (e.g. Ye Nwe Dam, Baing Dar Dam). As Myanmar becomes more developed, there is an increasing demand on hydropower and irrigation from the dams. The spatial proximity of the dams to active faults, both mapped and unmapped, represents an increased exposure to seismic hazard. When the source is sufficiently shallow and close, even events as small as M4 can produce large Peak Ground Acceleration (PGA) (e.g. Wei at al., 2015). Some cracks were detected on the downstream side of the dam body of the South Nawin Dam after two shallow M>4 earthquakes occurred at the western edge of the BYR in October 2018 and followed by smaller earthquakes until January 2019 (Tint Lwin Swe, 2019). The 2018 Mw 6.0 event did not cause damage to the nearby dams, possibly because the closest dam was more than 30 km away from the earthquake. In addition to damage due to natural earthquakes, large reservoirs with significant impounding capacity can also trigger seismicity on nearby faults, given favorable existing stress, permeability and pore fluid conditions (Talwani & Acree, 1984; ICOLD, 2011; Ellsworth, 2013; Foulger et al., 2018). Therefore, proximity to active faults and earthquake-resistant dam design are key factors in planning and construction of dams in the region. We therefore further discuss the attenuation of the ground motion produced by the 2018 Mw6.0 sequence.

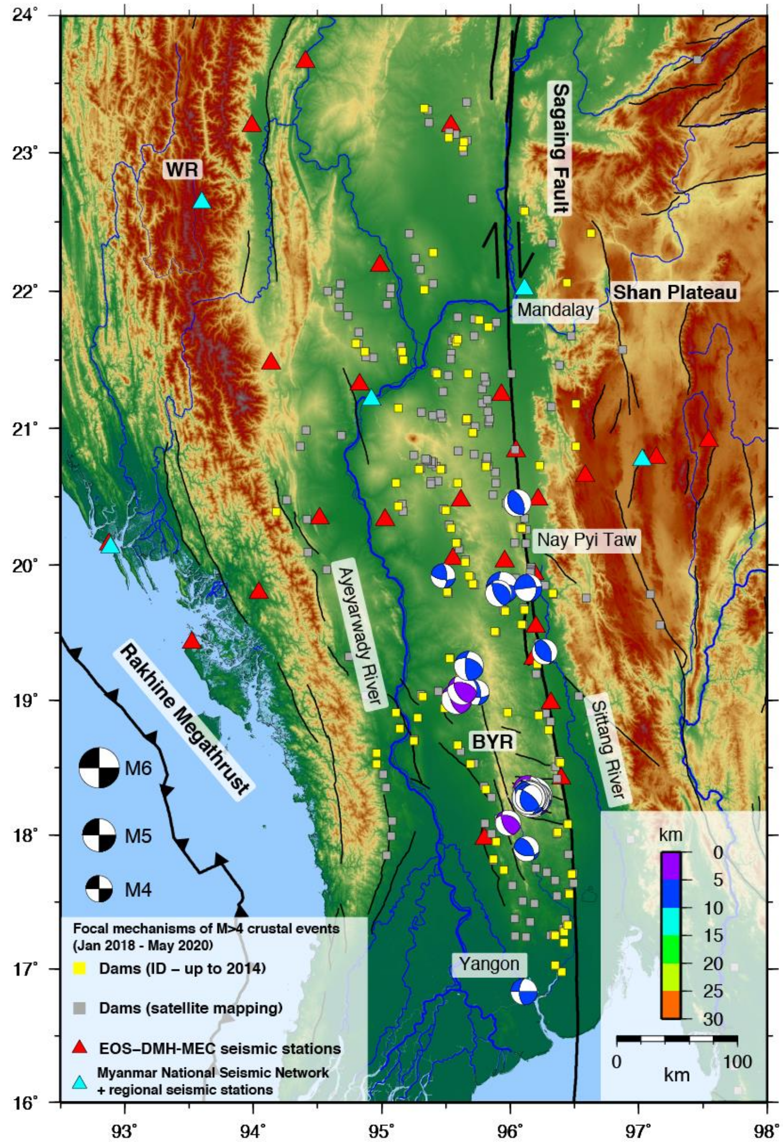

Figure 10. Distribution of dams and active crustal faults in Myanmar. Plot of focal mechanisms of M>4 crustal (<30 km deep) earthquakes from global earthquake catalogs and our inversion of events recorded by the EOS-DMH-MEC seismic stations. Dam locations provided from the Irrigation Department (ID) complete up to 2014 is indicated by the yellow squares while dam locations recently mapped from satellite imagery is indicated by gray squares. Active crustal seismicity within the BYR and along the Sagaing Fault, in close proximity to dams, suggest an increased seismic hazard to the population.

We plotted the PGA data for the mainshock (Mw6.0) and two early aftershocks (Mb5.2, Mw4.1) (Fig. 11), recorded by the broadband network and one strong motion station located at Phyu Dam, approximately 32 km away (white triangle in Fig. 8). We also plotted the PGA for several same-day M>4.3 aftershocks recorded by the strong motion seismometer. Since there is no Ground Motion Prediction Equation (GMPE) available in the region, we adopted the hard rock GMPE in Japan (Zhao et al., 2006) for comparison and discussion. As the mainshock waveforms were clipped at the nearest broadband stations, the strong motion station provides valuable nearfield data in assessing the performance of the GMPE. In general, we find that the GMPE can fit the mainshock PGAs quite well, but does poorly for the smaller aftershocks, especially at distances larger than 50 km. Since the site classifications are not yet available for these sites, we did not take them into account in the attenuation analysis, which would be a major cause of the scattering and deviations in Fig. 11. This is left for future efforts, which are critical for the seismic hazard assessment in Myanmar.

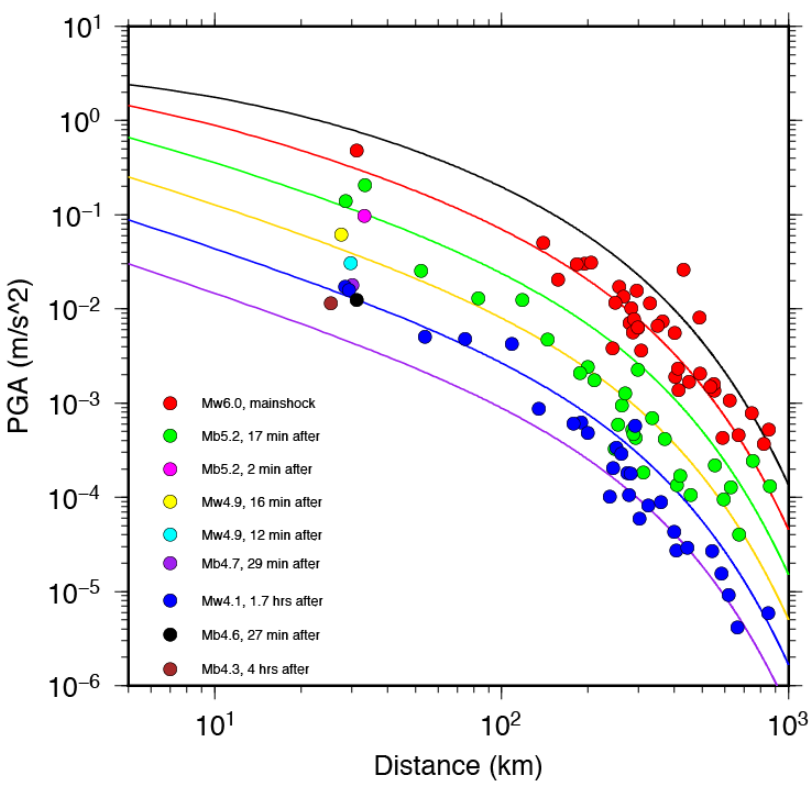

Figure 11. PGA analysis of the Mw6.0 Bago-Yoma earthquake sequence. Colored circles represent PGA observed at the Phyu Dam strong motion station and EOS-DMH-MEC broadband stations. The location of Phyu Dam is indicated by a white triangle in Figure 8. Colored lines represent the calculated PGA from the GMPE proposed by Zhao et al. (2006). The PGA for the Mw6.0 sequence is consistent with the GMPE, but deviates from the GMPE as the magnitude decreases.

4.3 Complicated structure underneath Myanmar

The seismic record of the mainshock shows complicated waveforms recorded at the seismic stations throughout Myanmar (Fig. S6). The Pnl segment shows multiple arrivals possibly from a mix of reflected and depth phases, making it difficult to determine the depth phases for constraining the focal depth (Fig 5b). The surface wave segment shows a relatively large amplitude coda that extends for tens of seconds for stations located on hard rock and longer for stations located within the Central Myanmar Basin (Fig. S6), as also revealed by a previous study (Wang et al., 2019). Therefore, a 1D velocity model is not able to adequately model the waveforms recorded at these stations at sufficiently high frequencies to replicate the complicated Pnl arrivals. However, the observed waveforms themselves provide several hints about the earthquake source. The long duration coda of the surface waves supports our shallow focal depth results, since earthquakes that nucleate at shallow depths are better able to produce high-amplitude and long-duration surface wave coda compared to those that nucleate at deeper depths. Aftershocks with thrust-faulting focal mechanisms located within ~2.5 km of each other along the A-A’ profile have similar waveforms as indicated by the high cross-correlation coefficient values (Fig 5b), thus, validating our focal mechanism inversion results and allow us to identify the moveout of possible depth phases. In addition, the observed surface-/Pnl-wave amplitude ratios between these events allow us to infer the relative depth of each event and support our depth inversion results that suggest a shallow SW-dipping fault. To model these broadband waveforms, better 2D or 3D velocity models are required.

5. Conclusions

We propose a fault geometry of (strike = 130˚, dip = 40˚) for the shallow thrust fault that ruptured during the 11th January 2018, Mw 6.0 Bago-Yoma earthquake in southern Myanmar. From high-resolution earthquake relocation and source parameter inversions, we infer that the mainshock ruptured the fault ~10km along strike, with thrusting aftershocks located at depths between 3-7 km. We also find that the mainshock triggered deeper (7-8 km) strike-slip aftershocks a few km to the east of the mainshock epicenter. Combined with InSAR observations, static slip inversion, depth-phase analysis, historical seismicity, and previous geologic studies, the results and observations support a thrust fault dipping to the SW at an angle of approximately 40˚, which we interpret to be a pre-existing fault within the BYR anticlinorium. Our findings highlight the complexity of the tectonics of southern Myanmar, where this earthquake sequence and several other M >4 crustal earthquakes in the region indicate ongoing distributed deformation between the oblique Rakhine megathrust and the dextral Sagaing Fault. With the development of more infrastructure such as dams within and surrounding the BYR, more high-resolution seismological studies on existing faults and potentially active intraplate faults and their associated hazards must be conducted.

Acknowledgments

This research is supported by the National Research Foundation Singapore and the Singapore Ministry of Education under the Research Centers of Excellence initiative via the Earth Observatory of Singapore (EOS) grant 04MNS001848A620. The EOS-DMH-MEC seismic data was accessed from the EOS Center for Geohazard Observation (CGO); we thank the CGO for installing and servicing the EOS-DMH-MEC seismic array. We are grateful to the Department of Meteorology and Hydrology of Myanmar and Myanmar Earthquake Committee for their help in installing the EOS-DMH-MEC seismic array. The EOS-DMH-MEC seismic waveform data used in this study can be accessed from (https://doi.org/10.21979/N9/BQ11DP) and the ALOS-2 InSAR data used in the static slip inversion can be accessed from (https://doi.org/10.21979/N9/QHJXU7). Seismic data from the MM and TM network were downloaded through the Incorporated Research Institutions for Seismology (IRIS) website (https://www.iris.edu/hq/). ALOS-2 SAR data were obtained from the Japanese Aerospace Agency (JAXA) under RA-6 project number 3240 awarded to E. Lindsey. Mapping of dams from satellite imagery was conducted using Google Earth. Sac 2000, Taup (Crotwell et al.., 1999), and GMT (Wessel et al.., 2013) were used for basic data processing and figure development. We are grateful to Kyle Bradley for useful discussions.

References

Bertrand, G., & Rangin, C. (2003). Tectonics of the western margin of the Shan plateau (central Myanmar): Implication for the India-Indochin oblique convergence since the Oligocene. *Journal of Asian Earth Sciences*, *21*(10), 1139–1157. https://doi.org/10.1016/S1367-9120(02)00183-9.

Bender, F., and D. N. Bannert (1983), Geology of Burma, Science Publishers, Gebruder Borntraeger Verlagsbuchhandlung.

Chen, C. W., & Zebker, H. A. (2000). Network approaches to two-dimensional phase unwrapping: intractability and two new algorithms: erratum. *Journal of the Optical Society of America A*, *17*(3), 401–414. https://doi.org/10.1364/josaa.18.001192.

Chen, W., & Molnar, P. (1990). Source parameters of earthquakes and intraplate deformation beneath the Shillong Plateau and Northern Indo-Burman Ranges. *Journal of Geophysical Research*, *95*(90), 12527–12552. https://doi.org/10.1029/JB095iB08p12527.

Chhibber, H. L., and R. Ramamirtham (1934), The geology of Burma, MacMillan, London, U. K.

Chit Tet Mon, Gong, X., Wen, Y., Jiang, M., & Chen, Q. F. (2020). Insight Into Major Active Faults in Central Myanmar and the Related Geodynamic Sources, *Geophysical Research Letters*, 47, 1–8. https://doi.org/10.1029/2019GL086236.

DeMets, C., Gordon, R. G., & Argus, D. F. (2010). Geologically current plate motions. *Geophysical Journal International*, *181*(1), 1–80. https://doi.org/10.1111/j.1365-246X.2009.04491.x.

Dziewonski, A. M., Chou, T. A., & Woodhouse, J. H. (1981). Determination of earthquake source parameters from waveform data for studies of global and regional seismicity. *Journal of Geophysical Research*, *86*(B4), 2825–2852. https://doi.org/10.1029/JB086iB04p02825.

Ekström, G., Nettles, M., & Dziewoński, A. M. (2012). The global CMT project 2004-2010: Centroid-moment tensors for 13,017 earthquakes. *Physics of the Earth and Planetary Interiors*, *200–201*, 1–9. https://doi.org/10.1016/j.pepi.2012.04.002

Ellsworth, W. L. (2013). Injection-Induced Earthquakes. *Science*, *341*, 1–8. https://doi.org/10.1126/science.1225942.

Foulger, G. R., Wilson, M. P., Gluyas, J. G., Julian, B. R., & Davies, R. J. (2018). Global review of human-induced earthquakes. *Earth-Science Reviews*, *178*(July 2017), 438–514. https://doi.org/10.1016/j.earscirev.2017.07.008.

Hrin Nei Thiam, Htwe, Y. M. M., Kyaw, T. L., Tun, P. P., Min, Z., Htwe, S. H., … Hough, S. E. (2017). A report on upgraded seismic monitoring stations in Myanmar: Station performance and site response. *Seismological Research Letters*, *88*(3), 926–934. https://doi.org/10.1785/0220160168.

Hurukawa, N., & Maung Maung, P. (2011). Two seismic gaps on the Sagaing Fault, Myanmar, derived from relocation of historical earthquakes since 1918. *Geophysical Research Letters*, *38*(1), 1–5. https://doi.org/10.1016/j.earscirev.2017.07.008.

ICOLD (International Commission on Large Dams) (2011). Reservoir and Seismicity: State of Knowledge. *International Commission on Large Dams Bulletin 137*, p. 1-110.

Jónsson, S., Zebker, H., Segall, P., & Amelung, F. (2002). Earthquake, Estimated from Satellite Radar and GPS Measurements. *Bulletin of the Seismological Society of America*, 92(4), 1377-1389. https://doi.org/10.1785/0120000922.

Laske, G., Masters., G., Ma, Z. and Pasyanos, M. (2013). Update on CRUST1.0 - A 1-degree Global Model of Earth's Crust, *Geophys. Res. Abstracts*, 15, Abstract EGU2013-2658.

Le Dain, A. Y., Tapponnier, P., & Molnar, P. (1984). Active Faulting and Tectonics of Burma and Surrounding Regions. *Journal of Geophysical Research*, *89*(B1), 453–472. https://doi.org/10.1029/JB089iB01p00453.

Mallick, R., Lindsey, E. O., Feng, L., Hubbard, J., Banerjee, P., & Hill, E. M. (2019). Active Convergence of the India-Burma-Sunda Plates Revealed by a New Continuous GPS Network. *Journal of Geophysical Research: Solid Earth*, *124*(3), 3155–3171. https://doi.org/10.1029/2018JB016480.

Maung Thein, Than Myint, Soe Thura Tun & Tint Lwin Swe (2009). Earthquake and tsunami hazard in Myanmar. *Journal of Earthquake and Tsunami*, *3*(2), 43–57. https://doi.org/10.1142/S1793431109000482.

Naing Maw Than, Khin, K., & Thein, M. (2017). Chapter 7: Cretaceous geology of Myanmar and Cenozoic geology in the Central Myanmar Basin. *Geological Society, London, Memoirs*, *48*(1), 143–167. https://doi.org/10.1144/m48.7.

NASA JPL (2013). NASA Shuttle Radar Topography Mission Global 1 arc second, distributed by NASA EOSDIS Land Processes DAAC, https://doi.org/10.5067/MEaSUREs/SRTM/SRTMGL1.003.

Ni, J. F., Guzman-Speziale, M., Bevis, M., Holt, W. E., Wallace, T. C., & Seager, W. R. (1989). Accretionary tectonics of Burma and the three-dimensional geometry of the Burma subduction zone. *Geology*, 17(1), 68–71. https://doi.org/10.1130/0091-7613(1989)017<0068:ATOBAT>2.3.CO;2

Oldham, T. (1883). A catalogue of Indian earthquakes from the earliest time to the end of A.D. 1869, Memoir. Geol. Surv. India, 29, 163–215.

Pace, P., & Calamita, F. (2014). Push-up inversion structures v. fault-bend reactivation anticlines along oblique thrust ramps: Examples from the Apennines fold-and-thrust belt (Italy). *Journal of the Geological Society*, *171*(2), 227–238. https://doi.org/10.1144/jgs2013-053.

Pivnik, D. A., Nahm, J., Tucker, R. S., Smith, G. O., Nyein, K., Nyunt, M., & Maung, P. H. (1998). Polyphase deformation in a fore-arc/back-arc basin, Salin subbasin, Myanmar (Burma). *AAPG Bulletin*, *82*(10), 1837–1856. https://doi.org/10.1306/1D9BD15F-172D-11D7-8645000102C1865D.

Rangin, C. (2017). Chapter 3: Active and recent tectonics of the Burma Platelet in Myanmar. *Geological Society, London, Memoirs*, *48*(1), 53–64. https://doi.org/10.1144/M48.3.

Ridd, M. F. & Racey, A. (2015). Chapter 4: Onshore petroleum geology of Myanmar : Central Burma Depression. *Geological Society, London, Memoirs,* 45(1), 21–50. https://doi.org/10.1144/M45.04.

Sandwell, D., Mellors, R., Tong, X., Wei, M., & Wessel, P. (2011). Open radar interferometry software for mapping surface deformation. *Eos, Transactions American Geophysical Union*, *92*(28), 234-235. https://doi.org/10.1029/2011EO280002.

Shinn, Y. J. (2015). Geological structures and controls on half-graben inversion in the western Gunsan Basin, Yellow Sea. *Marine and Petroleum Geology*, *68*, 480–491. https://doi.org/10.1016/j.marpetgeo.2015.09.013.

Shyu, J. B. H., Wang, C. C., Wang, Y., Shen, C. C., Chiang, H. W., Liu, S. C., … Tun, S. T. (2018). Upper-plate splay fault earthquakes along the Arakan subduction belt recorded by uplifted coral microatolls on northern Ramree Island, western Myanmar (Burma). *Earth and Planetary Science Letters*, *484*, 241–252. https://doi.org/10.1002/jgrb.50121.

Simons, M., Fialko, Y., & Rivera, L. (2002). Coseismic deformation from the 1999 Mw 7.1 Hector Mine, California, earthquake as inferred from InSAR and GPS observations. *Bulletin of the Seismological Society of America*, *92*(4), 1390–1402. https://doi.org/10.1785/0120000933.

Sloan, R. A., Elliott, J. R., Searle, M. P., & Morley, C. K. (2017). Chapter 2: Active tectonics of Myanmar and the Andaman Sea. *Geological Society, London, Memoirs*, *48*(1), 19–52. https://doi.org/10.1144/M48.2.

Socquet, A., Vigny, C., Chamot-Rooke, N., Simons, W., Rangin, C., & Ambrosius, B. (2006). India and Sunda plates motion and deformation along their boundary in Myanmar determined by GPS. *Journal of Geophysical Research: Solid Earth*, *111*(5), 1–11. https://doi.org/10.1029/2005JB003877.

Steckler, M. S., Akhter, S. H., & Seeber, L. (2008). Collision of the Ganges-Brahmaputra Delta with the Burma Arc: Implications for earthquake hazard. *Earth and Planetary Science Letters*, *273*(3–4), 367–378. https://doi.org/10.1016/j.epsl.2008.07.009.

Talwani, P., & Acree, S. (1984). Pore pressure diffusion and the mechanism of dams-induced seismicity. *Pure and Applied Geophysics PAGEOPH*, *122*(6), 947–965. https://doi.org/10.1007/BF00876395.

Taylor, M., & Yin, A. (2009). Active structures of the Himalayan-Tibetan orogen and their relationships to earthquake distribution, contemporary strain field, and Cenozoic volcanism. *Geosphere, 5*(3), 199–214. https://doi.org/10.1130/GES00217.1.

Tint Lwin Swe (2019). Importance of active tectonic studies of the Bago-Yoma anticlinorium for major civil engineering projects [Abstract]. *7th International Workshop on Seismotectonics in Myanmar and Earthquake Risk Management (SMERM 2019)*, 4-5.

Wang, Y., Shyu, J. B. H., Sieh, K., Chiang, H. W., Wang, C. C., Aung, T., … Tun, S. T. (2013). Permanent upper plate deformation in western Myanmar during the great 1762 earthquake: Implications for neotectonic behavior of the northern Sunda megathrust. *Journal of Geophysical Research: Solid Earth*, *118*(3), 1277–1303. https://doi.org/10.1002/jgrb.50121.

Wang, Y., Sieh, K., Soe, T. T., Lai, K.-Y., & Myint, T. (2014). Active tectonics and earthquake potential of the Myanmar region. *Journal of Geophysical Research: Solid Earth*, 3576–3822. https://doi.org/10.1002/2013JB010762

Wang, X., Wei, S., Wang, Y., Maung Maung, P., Hubbard, J., Banerjee, P., … Almeida, R. (2019). A 3-D Shear Wave Velocity Model for Myanmar Region. *Journal of Geophysical Research: Solid Earth*, 124, 1-23. https://doi.org/10.1029/2018JB016622

Wang, Y., Sieh, K., Aung, T., Min, S., Khaing, S. N., & Tun, S. T. (2011). Earthquakes and slip rate of the southern Sagaing fault: Insights from an offset ancient fort wall, lower Burma (Myanmar). *Geophysical Journal International*, *185*(1), 49–64. https://doi.org/10.1111/j.1365-246X.2010.04918.x

Wei, S., Avouac, J.P., Hudnut, K.W., Donnellan, A., Parker, J.W., Graves, R.W., Helmberger, D., Fielding, E., Liu, Z., Cappa, F. and Eneva, M., 2015. The 2012 Brawley swarm triggered by injection-induced aseismic slip. *Earth and Planetary Science Letters*, 422, pp.115-125. https://doi.org/10.1016/j.epsl.2015.03.054

Zhao, J. X., Zhang, J., Asano, A., Ohno, Y., Oouchi, T., Takahashi, T., … Fukushima, Y. (2006). Attenuation relations of strong ground motion in Japan using site classification based on predominant period. *Bulletin of the Seismological Society of America*, *96*(3), 898–913. https://doi.org/10.1785/0120050122

Zhu, L., & Ben-Zion, Y. (2013). Parametrization of general seismic potency and moment tensors for source inversion of seismic waveform data. *Geophysical Journal International*, *194*(2), 839–843. https://doi.org/10.1093/gji/ggt137

Zhu, L., & Helmberger, D. V. (1996). Advancement in source estimation techniques using broadband regional seismograms. *Bulletin of the Seismological Society of America*, *86*(5), 1634–1641. https://doi.org/10.1785/0120160029

Zhu, L., & Rivera, L. A. (2002). A note on the dynamic and static displacements from a point source in multilayered media. *Geophysical Journal International*, *148*, 619–627. https://doi.org/ https://doi.org/10.1046/j.1365-246X.2002.01610.x